Implementation of a Finite Difference Frequency Domain Mode Solver Incorporating Subpixel Smoothing

DIMITRIOS ALEXOPOULOS[1,*] AND THOMAS KAMALAKIS[1]

[1]*Department of Informatics and Telematics, Harokopio University, Omirou 9, 17778 Tavros, Greece*
[*]*alexopoulosd@hua.gr*

Abstract: Finite difference frequency domain (FDFD) mode solvers are straightforward to implement but can suffer from slow convergence when applied to high-contrast refractive index structures. In this work, we show how subpixel smoothing can improve the convergence properties of a full-vectorial FDFD mode solver. Based on a standard Yee grid, we formulate a generalized eigenbproblem whose solutions provide the modes of the waveguides taking into account the tensor nature of the effective dielectric constant. We investigate the convergence of the proposed FDFD mode solver in several cases including a step index fiber, a microsctuctured fiber and a cylindrical plasmonic waveguide. The results show that tensor smoothing can significantly improve the convergence of the solver thus allowing the use of less dense grids in the calculations. Our implementation is freely available on the web under an open-source licence.

© 2026 Optica Publishing Group

1. Introduction

Finite difference frequency domain (FDFD) [1] is an effective tool for simulating the behavior of photonic structures especially when lossy materials with frequency-dependent dielectric constant need to be studied [2]. Much like in its time-domain counterpart, the finite difference time domain (FDTD) method [3], in FDFD, Maxwell's equations are discretized in the *frequency* domain and the spatial derivatives of the field components are approximated by finite differences. There are two variants of the FDFD method: in the first variant, we seek to obtain the total electric and magnetic (EM) fields $\mathbf{E}$ and $\mathbf{H}$, respectively and hence we discretize Maxwell's equations describing the total EM field propagation inside a structure [4]. This results in a linear system of equations, the solution of which yields the EM field. In the second variant, we use FDFD to obtain the EM modes of the structure and therefore start from Maxwell's equations for the modes. This results in an algebraic eigenproblem, the eigenvalues and eigenvectors of which are related to the effective indices and the field distributions of the modes, respectively [5].

In order to discretize Maxwell's equations, one can adopt the Yee cell shown in Figure 1, where the field components are calculated at specific points in space which are chosen in a manner that simplifies the finite difference equations [6–8]. The Yee cell, which is also adopted in this work, has been used extensively in FDTD implementations [3] to provide second order accuracy and besides its simplicity, its adoption in FDFD mode solvers has the advantage that their results can be incorporated in an FDTD algorithm. However, it should be pointed out that non-Yee grids can also be considered leading to improved convergence. For example, in the work of [9–11], a combination of Taylor series expansion and generalized Douglas scheme has lead to significant improvement in truncation and relative error for several structures. In addition finite difference stencil implementation have been adopted in [12, 13], exhibiting very low relative error in plasmonic structures as well.

FDFD methods may require increased computational resources (e.g. in terms of computer memory) in the case of large structures or structures with fine salient features. The situation is further complicated in structures with discontinuities in their dielectric constant distribution ϵ.

Consider for example, a discontinuous ϵ distribution along an interface between two materials, as shown in Figure 1. Near the interface, e.g. at point A in the figure, there is some ambiguity regarding the value of ϵ to be used. For the grid choice shown in the figure, we are inclined to use $\epsilon = \epsilon_\mathrm{b}$ at A, but if the grid is slightly perturbed, point A can easily end up on the other side of the interface and hence its value would change to $\epsilon = \epsilon_\mathrm{a}$. If the contrast $\Delta\epsilon = |\epsilon_\mathrm{b} - \epsilon_\mathrm{a}|$ is large, this will undermine the convergence of FDFD. This problem can be mitigated to an extent, by adopting a dielectric smoothing scheme where ϵ is properly averaged around point A. For a rectangular grid, we may consider the area S around A in Figure 1, with corners at $(x_A \pm \Delta x/2, y_A \pm \Delta y/2)$ where (x_A, y_A) are the coordinates of A and $\Delta x/2$ and $\Delta y/2$ is the spacing between grid points along the x and y axis, respectively and use the following averaged value of ϵ at A:

$$\langle \epsilon \rangle = \frac{1}{S} \int_S \epsilon(\mathbf{r}) \mathrm{d}S \tag{1}$$

This however, turns out to be sub-optimal. In fact, when computing the electric field $\mathbf{E} = \epsilon^{-1}\mathbf{D}$ from the electric displacement field $\mathbf{D}$ [14] near a dielectric interface with surface normal $\hat{n}$, it is better to use $\langle \epsilon(\mathbf{r}) \rangle$ for electric field components $\mathbf{E} || \hat{n}$ and $1/\langle 1/\epsilon(\mathbf{r}) \rangle$ for $\mathbf{E} \perp \hat{n}$ [15]. This is equivalent to using an effective inverse dielectric tensor in Maxwell's equations:

$$\overline{\overline{\epsilon^{-1}}} = \left\langle \epsilon^{-1} \right\rangle \overline{\overline{P}} + \langle \epsilon \rangle^{-1} \left(\overline{\overline{I}} - \overline{\overline{P}} \right) \tag{2}$$

where $\overline{\overline{P}}$ is the projection matrix along $\hat{n}$, with elements $P_{ij} = n_i n_j$ and $\overline{\overline{I}}$ is the identity matrix.

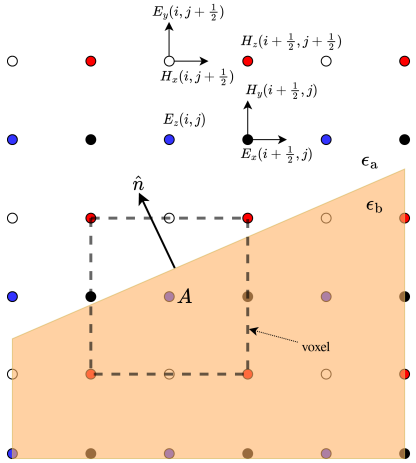

Fig. 1. An example of a dielectric interface in the Yee cell between two materials with dielectric constants ϵ_a and ϵ_b.

The electric field is then determined by the following constitutive relation:

$$\mathbf{E} = \overline{\overline{\epsilon^{-1}}} \mathbf{D} \tag{3}$$

This *effective dielectric tensor* smoothing technique has demonstrated improved convergence when applied to FDTD [16] simulations. It has also been successfully tested for solving Maxwell's equations to obtain the total EM field inside a structure using FDFD [4]. In the current work, we show how it can also be applied to improve the accuracy of an FDFD mode solver. Starting from Maxwell's equations in the frequency domain and using finite differences, we show how an algebraic eigenproblem can be derived, taking into account (3). Due to the tensor nature of

(3), this turns out to be a *generalized* eigenproblem. We use interpolation to obtain the missing off-diagonal field components at the various grid points. Using the obtained eigenproblem, we implement a `Python`-based mode solver and apply it to various structures to ascertain its accuracy, including a simple step-index fiber, a micro-structured fiber and a plasmonic waveguide. In all examples considered, tensor smoothing yields improved convergence compared to the case of no or scalar smoothing. To the best of the authors' knowledge, this is the first time such a scheme has been combined with an FDFD mode solver. Our implementation is freely available on the web [17], under an open-source licence. The rest of the paper is organized as follows: In Section 2, we discuss the derivation of the generalized eigenproblem in detail, starting from the modal equations and incorporating tensor smoothing and off-diagonal field component interpolation. We also highlight some further implementation details of the mode solver. In Section 3, we apply the mode solver to study some example waveguide structures and compare its accuracy against other smoothing strategies. Some concluding remarks are given in Section 4.

2. Eigenproblem Formulation

2.1. Maxwell's equations in the frequency domain

In order to formulate the eigenproblem, we start from Maxwell's equations in the frequency domain. Assuming that the waveguide is uniform along the propagation direction z and that the EM field has an $\propto \mathrm{e}^{j\omega t}$ time dependence, we readily obtain the following equations for the EM field [14]:

$$\nabla \times \mathbf{E} = -j\omega\mu_0\mathbf{H} \tag{4a}$$

$$\nabla \times \mathbf{H} = j\omega\mathbf{D} \tag{4b}$$

In (4), $\mathbf{E}$ and $\mathbf{H}$ is the electric and magnetic field components of the mode, that can be written as:

$$\mathbf{E}(\mathbf{r}) = \mathbf{e}(x, y)\mathrm{e}^{-j\beta z} \tag{5a}$$

$$\mathbf{H}(\mathbf{r}) = \mathbf{h}(x, y)\mathrm{e}^{-j\beta z} \tag{5b}$$

In equations (4)-(5), ω and β are the angular frequency and propagation constant of the mode respectively, while μ_0 is the vacuum permeability. The effective refractive index n_{eff} of the mode is related to β through $\beta = 2\pi n_{\mathrm{eff}}/\lambda$ where λ is the wavelength. The electric field displacement $\mathbf{D}$ also has an $\mathrm{e}^{-j\beta z}$ spatial dependence, i.e.

$$\mathbf{D}(\mathbf{r}) = \mathbf{d}(x, y)\mathrm{e}^{-j\beta z} \tag{6}$$

Equations (4) and (5) along with (3) and (6) form the basis from which the eigenvalue problem will be derived. Substituting (5) and (6) in (4) and using the fact that $\partial/\partial z \rightarrow -j\beta$, we readily obtain the following equations for the field components:

$$\frac{\partial e_z}{\partial y} + j\beta e_{\mathrm{y}} = -j\omega\mu_0 h_x \tag{7a}$$

$$\frac{\partial e_z}{\partial x} + j\beta e_{\mathrm{x}} = j\omega\mu_0 h_y \tag{7b}$$

$$\frac{\partial e_y}{\partial x} - \frac{\partial e_x}{\partial y} = -j\omega\mu_0 h_z \tag{7c}$$

$$\frac{\partial h_z}{\partial y} + j\beta h_{\mathrm{y}} = j\omega d_x \tag{8a}$$

$$\frac{\partial h_z}{\partial x} + j\beta h_x = -j\omega d_y \tag{8b}$$

$$\frac{\partial h_y}{\partial x} - \frac{\partial h_x}{\partial y} = j\omega d_z \tag{8c}$$

2.2. Subpixel smoothing

For uniform waveguides, the dielectric interfaces will also be uniform in z direction, implying that the perpendicular vector $\hat{n}$ in Figure 1, will not have a z component, i.e. $\hat{n} = (n_x, n_y, 0)$ and hence the inverse dielectric tensor in (2), is reduced to:

$$\overline{\overline{\epsilon^{-1}}} = \begin{bmatrix} \tau_{xx} & \tau_{xy} & 0 \\ \tau_{yx} & \tau_{yy} & 0 \\ 0 & 0 & \tau_{zz} \end{bmatrix} \tag{9}$$

where the tensor elements are determined by:

$$\tau_{xx} = n_x^2 \langle \epsilon^{-1} \rangle + n_y^2 \langle \epsilon \rangle^{-1} \tag{10a}$$

$$\tau_{yy} = n_y^2 \langle \epsilon^{-1} \rangle + n_x^2 \langle \epsilon \rangle^{-1} \tag{10b}$$

$$\tau_{xy} = \tau_{yx} = n_y n_x (\langle \epsilon^{-1} \rangle - \langle \epsilon \rangle^{-1}) \tag{10c}$$

$$\tau_{zz} = \langle \epsilon \rangle^{-1} \tag{10d}$$

Using (3) and (9), we can write the following relation between the components of $\mathbf{e}$ and $\mathbf{d}$:

$$e_x = \tau_{xx} d_x + \tau_{xy} d_y \tag{11a}$$

$$e_y = \tau_{yx} d_x + \tau_{yy} d_y \tag{11b}$$

$$e_z = \tau_{zz} d_z \tag{11c}$$

Note that, in the case of no dielectric interface, ϵ is constant inside S and therefore $\left\langle \epsilon^{-1} \right\rangle = \langle \epsilon \rangle^{-1}$. In this case the off diagonal components vanish and the dielectric tensor is simply a product of the inverse scalar dielectric constant ϵ^{-1} and the identity matrix, leading to a scalar relation $\mathbf{e} = \epsilon^{-1}\mathbf{d}$.

2.3. Finite difference equations

Equations (7), (8) and (11) can be used to derive the finite difference equations. Figure 1 illustrates the Yee cell structure [18] adopted in this work. Note that the modal fields in (5) have an explicit $e^{-j\beta z}$ and hence the z-dependence does not need to be considered. In this case, Maxwell's equations need to be discretized along x and y only. As a consequence, the Yee cell in Figure 1, is two-dimensional and in some points, the field components overlap. The cell is formed starting from an initial grid of points (x_i, y_k) with $x_i = i\Delta x$ and $y_k = j\Delta y$ with $0 \leq i < N_x$ and $0 \leq k < N_y$ and i and k are integers. The Yee cell also contains intermediate points corresponding to half-integer values of i and k. Figure 1 shows where the EM field components are calculated along the grid and each component is calculated at $N_x \times N_y$ points. The electric field displacement components d_x, d_y and d_z are calculated at the same grid points as e_x, e_y and e_z respectively. To simplify the notation, we omit Δx and Δy when writing down

the field components in the finite difference equations. For example, $e_y(i, k+\frac{1}{2})$ denotes e_y calculated at $(i\Delta x, (k+\frac{1}{2})\Delta y)$ and so forth. We readily obtain from (7) and (8):

$$\frac{e_z(i,k+1)-e_z(i,k)}{\Delta y} + j\beta e_y(i,k+\tfrac{1}{2}) = -j\omega\mu_0 h_x(i,k+\tfrac{1}{2}) \tag{12a}$$

$$\frac{e_z(i+1,k)-e_z(i,k)}{\Delta x} + j\beta e_x(i+\tfrac{1}{2},k) = j\omega\mu_0 h_y(i+\tfrac{1}{2},k) \tag{12b}$$

$$\frac{e_y(i+1,k+\frac{1}{2})-e_y(i,k+\frac{1}{2})}{\Delta x} - \frac{e_x(i+\frac{1}{2},k+1)-e_x(i+\frac{1}{2},k)}{\Delta y} = - j\omega\mu_0 h_z(i+\tfrac{1}{2},k+\tfrac{1}{2}) \tag{12c}$$

$$\frac{h_z(i+\frac{1}{2},k+\frac{1}{2})-h_z(i+\frac{1}{2},k-\frac{1}{2})}{\Delta y} + j\beta h_y(i+\tfrac{1}{2},k) = j\omega d_x(i+\tfrac{1}{2},k) \tag{13a}$$

$$\frac{h_z(i+\frac{1}{2},k+\frac{1}{2})-h_z(i-\frac{1}{2},k+\frac{1}{2})}{\Delta x} + j\beta h_x(i,k+\tfrac{1}{2}) = -j\omega d_y(i,k+\tfrac{1}{2}) \tag{13b}$$

$$\frac{h_y(i,k+\frac{1}{2})-h_y(i,k-\frac{1}{2})}{\Delta y} - \frac{h_x(i+\frac{1}{2},k)-h_x(i-\frac{1}{2},k)}{\Delta x} = j\omega d_z(i,k) \tag{13c}$$

The constitutive equations in (9) are written as:

$$e_x(i+\tfrac{1}{2},k) = \tau_{xx}(i+\tfrac{1}{2},k)d_x(i+\tfrac{1}{2},k) + \tau_{xy}(i+\tfrac{1}{2},k)d_y(i+\tfrac{1}{2},k) \tag{14a}$$

$$e_y(i,k+\tfrac{1}{2}) = \tau_{yx}(i,k+\tfrac{1}{2})d_x(i,k+\tfrac{1}{2}) + \tau_{xy}(i,k+\tfrac{1}{2})d_y(i,k+\tfrac{1}{2}) \tag{14b}$$

$$e_z(i,k) = \tau_{zz}(i,k)d_z(i,k) \tag{14c}$$

2.4. Off-diagonal component interpolation

Note that (14a) requires d_y at $(i+\frac{1}{2},k)$ but according to Section 2.2, d_y is estimated at $(i,k+\frac{1}{2})$ instead. We adopt an interpolation method shown in Figure 1 [19]. The approximation used for d_y at $(i+\frac{1}{2},k)$ is:

$$\tau_{xy}(i+\tfrac{1}{2},k)d_y(i+\tfrac{1}{2},k) \approx \frac{1}{4}\left(d_y(i,k+\tfrac{1}{2})\tau_{xy}(i,k+\tfrac{1}{2}) + d_y(i,k-\tfrac{1}{2})\tau_{xy}(i,k-\tfrac{1}{2})\right) + \frac{1}{4}\left(d_y(i+1,k+\tfrac{1}{2})\tau_{xy}(i+1,k+\tfrac{1}{2}) + d_y(i+1,k-\tfrac{1}{2})\tau_{xy}(i+1,k-\tfrac{1}{2})\right) \tag{15}$$

A similar equation can be used at (14b) for approximating d_x at $(i,k+\frac{1}{2})$:

$$\tau_{yx}(i,k+\tfrac{1}{2})d_x(i,k+\tfrac{1}{2}) \approx \frac{1}{4}\left(d_x(i+\tfrac{1}{2},k)\tau_{yx}(i+\tfrac{1}{2},k) + d_x(i-\tfrac{1}{2},k)\tau_{yx}(i-\tfrac{1}{2},k)\right) + \frac{1}{4}\left(d_y(i+\tfrac{1}{2},k+1)\tau_{xy}(i+\tfrac{1}{2},k+1) + d_y(i-\tfrac{1}{2},k+1)\tau_{xy}(i-\tfrac{1}{2},k+1)\right) \tag{16}$$

Equations (12), (13) along with (14), (15), (16) can be used in order to derive the generalized eigenproblem that determines the modal fields and the effective indices of the modes.

2.5. Numerical smoothing

To speed up the computations, we need to efficiently perform subpixel smoothing at grid points that are near an interface, such as point A in Figure 1. We adopted a scheme where we first perform coarse averaging around each point (x, y) of the Yee grid, by considering the values of ϵ at $(x \pm \frac{1}{2}\Delta x, y \pm \frac{1}{2}\Delta y)$. If the average of these four values is different from $\epsilon(x, y)$, we assume that the point (x, y) is near an interface and apply finer averaging on an inner grid of 10×10 point around (x, y) to obtain $\langle\epsilon\rangle$ and $\left\langle\epsilon^{-1}\right\rangle$. In the case of point A in Figure 1, this inner grid lies inside S. At such points, we also calculate the normal vector $\hat{n}$ using numerical integration by considering equidistant points (x_u, y_u) on a circle circumference C around (x, y) with radius $R = \min\{\Delta x, \Delta y\}$. The normal vectors can be approximated by the line integral:

$$\hat{n} \propto \int_C \Delta\mathbf{r}\epsilon(\mathbf{r})\mathrm{d}l \tag{17}$$

where $\Delta\mathbf{r} = (x_u - x, y_u - y)$. This is a 2D analogue of the approach adopted in 3D plane wave expansion calculations [15]. In our implementations, we have simply summed 100 values of the integrand over equidistant points on S, to approximate the line integral.

2.6. Matrix equations

To derive the eigenproblem, we first need to arrange the $N_x \times N_y$ array values of each field component in column vectors. This is done by sequentially filling the elements of the vectors with the rows of the array. For example, the elements of the column vector $\mathbf{e}_z = [e'_z(p)]$ for $0 \le p < N_x N_y$ are calculated as $e'_z(p) = e_z(i, k)$ where $p = kN_x + i$. Using this notation, equation (12) is written in matrix form as:

$$\mathbf{U}_y\mathbf{e}_z + j\beta\mathbf{e}_y = -j\omega\mu_0\mathbf{h}_x \tag{18a}$$

$$\mathbf{U}_x\mathbf{e}_z + j\beta\mathbf{e}_x = j\omega\mu_0\mathbf{h}_y \tag{18b}$$

$$\mathbf{U}_x\mathbf{e}_y - \mathbf{U}_y\mathbf{e}_x = -j\omega\mu_0\mathbf{h}_z \tag{18c}$$

In (18), the matrices $\mathbf{U}_x$ and $\mathbf{U}_y$ are given by:

$$[\mathbf{U}_x]_{pq} = \Delta x^{-1}(\delta_{p,q-N_y} - \delta_{p,q}) \tag{19}$$

$$[\mathbf{U}_y]_{pq} = \Delta y^{-1}(\delta_{p,q-1} - \delta_{p,q}) \tag{20}$$

where $\delta_{pq} = 1$ if $p = q$ and $\delta_{pq} = 0$ if $p \ne q$. Equations (13) can be written in matrix form as:

$$\mathbf{V}_y\mathbf{h}_z + j\beta\mathbf{h}_y = j\omega\mathbf{d}_x \tag{21a}$$

$$\mathbf{V}_x\mathbf{h}_z + j\beta\mathbf{h}_x = -j\omega\mathbf{d}_y \tag{21b}$$

$$\mathbf{V}_x\mathbf{h}_y + \mathbf{V}_y\mathbf{h}_x = j\omega\mathbf{d}_z \tag{21c}$$

In equations (21), we have defined the matrices:

$$[\mathbf{V}_x]_{pq} = \Delta x^{-1}(\delta_{p,q} - \delta_{p,q+N_y}) \tag{22}$$

$$[\mathbf{V}_y]_{pq} = \Delta y^{-1}(\delta_{p,q} - \delta_{p,q+1}) \tag{23}$$

The constitutive relations (14) can be written in matrix forms as:

$$\mathbf{e}_x = \mathbf{T}_{xx}\mathbf{d}_x + \mathbf{T}_{xy}\mathbf{d}_y \tag{24a}$$

$$\mathbf{e}_y = \mathbf{T}_{yx}\mathbf{d}_x + \mathbf{T}_{yy}\mathbf{d}_y \tag{24b}$$

$$\mathbf{e}_z = \mathbf{T}_{zz}\mathbf{d}_z \tag{24c}$$

where we have defined the matrices:

$$[\mathbf{T}_{xx}]_{pq} = \tau_{xx}(i+\tfrac{1}{2},k)\delta_{p,q} \tag{25a}$$

$$[\mathbf{T}_{yy}]_{pq} = \tau_{yy}(i,k+\tfrac{1}{2})\delta_{p,q} \tag{25b}$$

$$[\mathbf{T}_{xy}]_{pq} = \frac{1}{4}\tau_{xy}(i,k+\tfrac{1}{2})(\delta_{p,q}+\delta_{p,q-N_y}+\delta_{p,q+1}+\delta_{p,q-N_y+1}) \tag{25c}$$

$$[\mathbf{T}_{yx}]_{pq} = \frac{1}{4}\tau_{yx}(i+\tfrac{1}{2},k)(\delta_{p,q}+\delta_{p,q+N_y}+\delta_{p,q-1}+\delta_{p,q+N_y-1}) \tag{25d}$$

$$[\mathbf{T}_{zz}]_{pq} = \tau_{zz}(i,k)\delta_{p,q} \tag{25e}$$

2.7. Eigenproblem formulation

By applying some algebra in equations (18), (21), (24), we derive the following generalized eigenproblem:

$$\begin{bmatrix}\mathbf{Q}_{xx} & \mathbf{Q}_{xy}\\ \mathbf{Q}_{yx} & \mathbf{Q}_{yy}\end{bmatrix}\begin{bmatrix}\mathbf{h}_x\\ \mathbf{h}_y\end{bmatrix} = \beta^2\begin{bmatrix}\mathbf{T}_{yy} & -\mathbf{T}_{yx}\\ -\mathbf{T}_{xy} & \mathbf{T}_{xx}\end{bmatrix}\begin{bmatrix}\mathbf{h}_x\\ \mathbf{h}_y\end{bmatrix} \tag{26}$$

where the submatrices are given by:

$$\mathbf{Q}_{xx} = \omega^2\mathbf{I} + \mathbf{U}_y\mathbf{T}_{zz}\mathbf{V}_y - \mathbf{T}_{yx}\mathbf{V}_y\mathbf{U}_x + \mathbf{T}_{yy}\mathbf{V}_x\mathbf{U}_x \tag{27a}$$

$$\mathbf{Q}_{yy} = \omega^2\mathbf{I} + \mathbf{U}_x\mathbf{T}_{zz}\mathbf{V}_x - \mathbf{T}_{xy}\mathbf{V}_x\mathbf{U}_y + \mathbf{T}_{xx}\mathbf{V}_yU_y \tag{27b}$$

$$\mathbf{Q}_{xy} = -\mathbf{U}_y\mathbf{T}_{zz}\mathbf{V}_x - \mathbf{T}_{yx}\mathbf{V}_y\mathbf{U}_y + \mathbf{T}_{yy}\mathbf{V}_x\mathbf{U}_y \tag{27c}$$

$$\mathbf{Q}_{yy} = -\mathbf{U}_x\mathbf{T}_{zz}\mathbf{V}_y - \mathbf{T}_{xy}\mathbf{V}_x\mathbf{U}_x + \mathbf{T}_{xx}\mathbf{V}_y\mathbf{U}_x \tag{27d}$$

Equations (26) and (27) constitute a generalized eigenproblem that can be solved to yield the propagation constants β and the field components of the modes. The submatrices in (27) are sparse and hence the eigenproblem can be solved using established numerical techniques [20]. Our `Python` implementation is based on the standard `numpy` and `scipy` modules and is available on the web [17] under an open-source licence.

3. Results and Discussion

In this section, we apply the implemented FDFD mode solver to study some indicative waveguide structures. Section 3.1 presents the results for a conventional step index fiber where the analytical solution for the mode effective refractive index n_{eff} is known [21]. We also consider a micro-structured fiber in Section 3.2 and a cylindrical plasmonic waveguide in Section 3.3. To ascertain the accuracy of tensor smoothing, we also investigate three additional smoothing schemes. In alternative A, we do not apply any smoothing, in which case the dielectric tensor in (9) is simply reduced to:

$$\overline{\overline{\epsilon^{-1}}} = \epsilon^{-1}\overline{\overline{I}} \tag{28}$$

In schemes B and C we consider only the diagonal elements of the dielectric tensor obtained by either smoothing ϵ and or ϵ^{-1} respectively. The tensor in (9) is therefore written as:

$$\overline{\overline{\epsilon^{-1}}} = \langle\epsilon\rangle^{-1}\,\overline{\overline{I}} \tag{29}$$

for alternative B and

$$\overline{\overline{\epsilon^{-1}}} = \left\langle \epsilon^{-1} \right\rangle \bar{\bar{I}} \tag{30}$$

for alternative C. We compare the convergence of these three alternative schemes against tensor smoothing (alternative D), where $\overline{\overline{\epsilon^{-1}}}$ is determined by (2).

3.1. Step-Index Fiber

We start our analysis with a step index fiber shown in Figure 2, which can serve as a reference case, since n_{eff} is known in closed form [21]. As in [5], we assume a fiber core radius $r_1 = 3$ μm, a core refractive index $n_1 = 1.45$ while the surrounding material has refractive index $n_2 = 1$. The wavelength of operation is $\lambda = 1.5$ μm and the computational window $L_x = L_y$ is 15μm. Figure 3, shows the values of n_{eff} obtained by varying N_x and setting $N_y = N_x$ for the four smoothing alternatives considered. We also show the analytical value for n_{eff} which is equal to $n^0_{\text{eff}} = 1.438604$.

It is evident that without any smoothing (alternative A), n_{eff} exhibits large fluctuations and hence convergence is poor. the solution exhibits much slower convergence. Also smoothing $1/\epsilon$ (alternative C) leads to reduced accuracy at small grid resolutions. Both smoothing (alternative D) and smoothing $1/\epsilon$ (alternative B) result in a better convergence behavior with the former being closer to the analytic solution. Clearly, alternative D is the method of choice for estimating n_{eff}. In the case of the step-index fiber where the analytical solution is known, it is interesting to

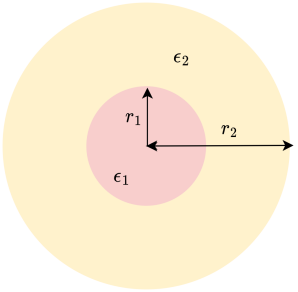

Fig. 2. A step index fiber waveguide.

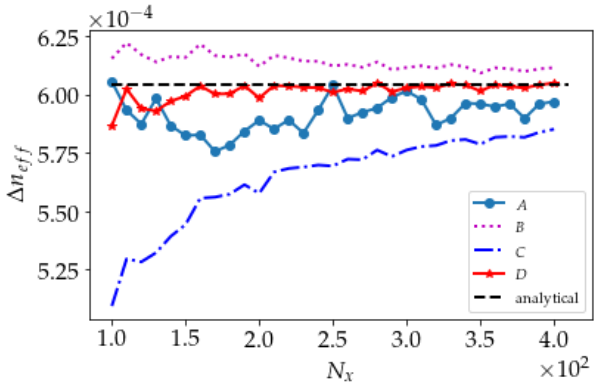

Fig. 3. Effective refractive index values around 1.438 for a step index fiber assuming different grid resolutions and four alternatives: $A \rightarrow$ no smoothing, $B \rightarrow$ smoothing of ϵ, $C \rightarrow$ smoothing of ϵ^{-1} and $D \rightarrow$ tensor smoothing.

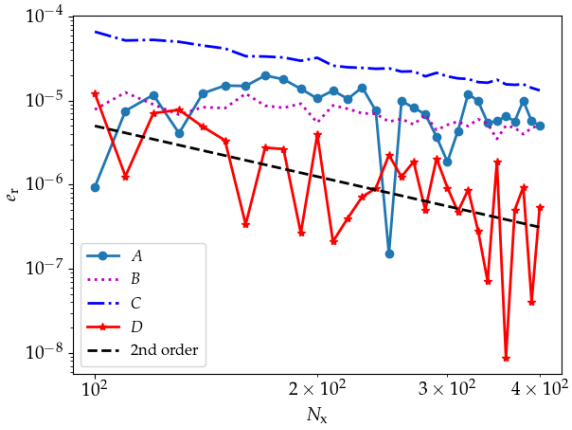

Fig. 4. Relative Error for step index fiber assuming different grid resolutions and four alternatives: $A \rightarrow$ no smoothing, $B \rightarrow$ smoothing of ϵ, $C \rightarrow$ smoothing of ϵ^{-1} and $D \rightarrow$ tensor smoothing. Quadratic convergence is also plotted with a dashed line.

plot the relative error, e_r

$$e_r = \frac{n_{\text{eff}} - n^0_{\text{eff}}}{n^0_{\text{eff}}} \tag{31}$$

with respect to N_x, shown in Figure 4. We also plot an ideal quadratic dependence, $\propto 1/N_x^2$, with a dashed black line. The figure is in agreement with [15] which suggests that subpixel smoothing method exhibits quadratic convergence.

3.2. Microstructured Optical Fiber

We also consider a more sophisticated dielectric waveguide example in Figure 5, which depicts an air-hole assisted optical fiber (AHAOF) [22]. The waveguide cross-section consists of air holes ($\epsilon_b = 1$) surrounding a higher index guiding core at the center ($\epsilon_a = n_a^2$ with $n_a = 1.45$). The holes and the core are embedded in a silica cladding with $\epsilon_c = n_c^2$ and $n_c = 1.42$. We assume that both core and hole radii are $r_b = r_a = 2\mu$m, while the distance between the center of the holes located at opposite sides with respect to the core is $2\Lambda = 5\mu$m and the computational window $L_x = L_y$ is 20μm. Using multipole analysis, the effective index was calculated at n_{eff}=1.4353607 at $\lambda = 1.5\mu$m [5].

Figure 6 shows the values of the effective index n_{eff} calculated by the FDFD mode solver assuming the four smoothing alternatives previously discussed. As expected, the convergence of the results in the no smoothing alternative A is very poor. Also, much like in the case of the step index fiber in Figure 2, the effective index obtained by the subpixel smoothing (alternative D), lies in between the values obtained by alternatives B and C corresponding to subpixel smoothing ϵ and ϵ^{-1} respectively. We also note that alternative D generally lies closer to the estimate obtained by multipole analysis (n_{eff}=1.4353607). For example, at $N_x = 120$, we obtain the following values of n_{eff}: 1.43537612 for alternative A, 1.43533334 for alternative B, 1.4353729 for alternative C and 1.4353602 for alternative D.

3.3. Cylindrical Hybrid Plasmonic Waveguide

We next consider a cylindrical hybrid plasmonic waveguide [23] depicted in Figure 7. The structure is comprised of a metallic core of radius $r_m = 100$nm with refractive index $n_m =$

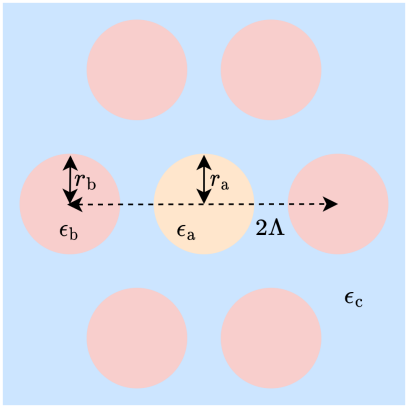

Fig. 5. A microstructured optical fiber.

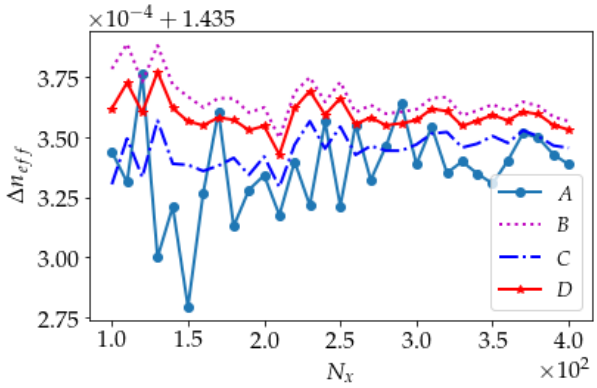

Fig. 6. Effective refractive index values around 1.435 for an AHAOF fiber assuming different grid resolutions and four alternatives: $A \rightarrow$ no smoothing, $B \rightarrow$ smoothing of ϵ, $C \rightarrow$ smoothing of ϵ^{-1} and $D \rightarrow$ tensor smoothing.

$0.1453 + j11.3587$, surrounded by a silica layer of thickness $w_1 = 50$nm with refractive index $n_1 = 1.445$. An outer silicon layer is also considered with thickness $w_2 = 200$nm and refractive index $n_2 = 3.455$, while the waveguide structure is embedded in silica. The operation wavelength is $\lambda = 1.55\mu$m and the computational window $L_x = L_y$ is 1.5μm.

The results obtained by the four subpixel smoothing alternatives are shown in Figure 8. Note that, subpixel smoothing is performed only on the real part of ϵ. Alternative B converges slowly in this case while convergence is better for alternative C. Alternative A exhibits high fluctuations while alternative D converges much faster than the rest of the alternatives in this case as well. The results match well with those reported on [23]. We have also considered applying subpixel smoothing in both the real and imaginary parts of ϵ rather than just the real part and the obtained results are shown in Figure 9. It is evident that subpixel smoothing both the real and imaginary parts has a negative effect on convergence since the fluctuations of n_{eff} are higher in this case.

4. Conclusion

In this paper, we discussed the effectiveness of tensor subpixel smoothing in full vectorial FDFD mode solver for general waveguiding structures. Based on a standard Yee grid formulation, we derived a generalized eigenbproblem, the solutions of which provide the properties of the

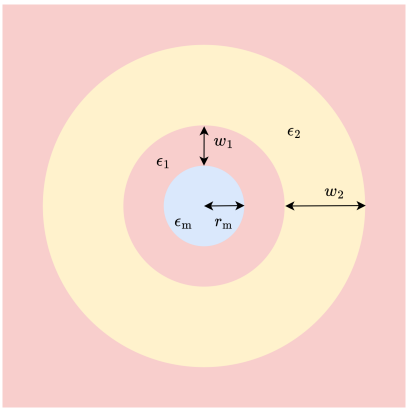

Fig. 7. A cylindrical hybrid plasmonic waveguide

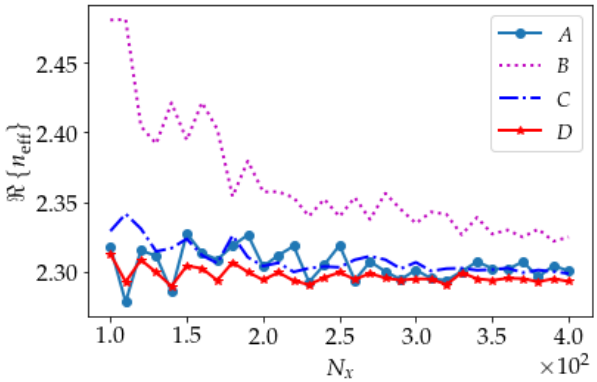

Fig. 8. Real part of the effective refractive for a cylindrical hybrid plasmonic waveguide assuming different grid resolutions and four alternatives: $A \rightarrow$ no smoothing, $B \rightarrow$ smoothing of ϵ, $C \rightarrow$ smoothing of ϵ^{-1} and $D \rightarrow$ tensor smoothing.

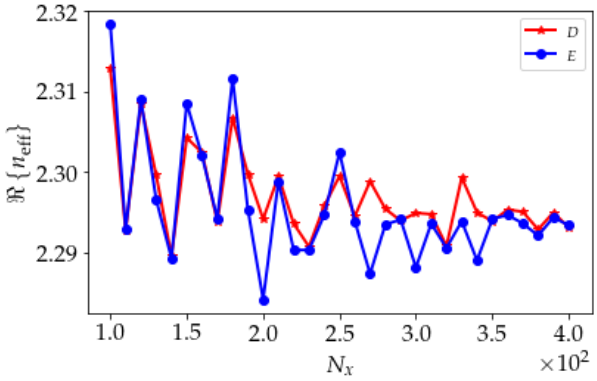

Fig. 9. Real part of the effective index values obtained by subpixel smoothing on either just the real part of ϵ (alternative D) or both the real and imaginary parts (alternative E).

waveguide modes. We discuss several implementation details of the mode solver and ascertain its convergence properties in dielectric and plasmonic waveguide examples. We also compare it against other smoothing strategies. In all examples considered, we show that tensor subpixel smoothing significantly improves the convergence of the FDFD solver, yielding accurate values for the effective index without requiring a dense grid. The `Python` code of our implementation is freely available on the web under an open-source licence.

5. Backmatter

Disclosures. The authors declare no conflicts of interest.

References

1. F. Xu, Y. Zhang, W. Hong, K. Wu, and T. J. Cui, "Finite-difference frequency-domain algorithm for modeling guided-wave properties of substrate integrated waveguide," IEEE Transactions on Microw. Theory Tech. **51**, 2221–2227 (2003).
2. D. Wu, R. Ohnishi, R. Uemura, T. Yamaguchi, and S. Ohnuki, "Finite-difference complex-frequency-domain method for optical and plasmonic analyses," IEEE Photonics Technol. Lett. **30**, 1024–1027 (2018).
3. A. Taflove and S. C. Hagness, *Finite-Difference Time-Domain Method* (Artech house, 2005).
4. A. N. Glytsis, A. D. Ppapadopoulos, and T. T. Koutserimpas, "Review and accuracy comparison of various permittivity-averaging schemes for material discontinuities in the two-dimensional fdfd method: implementation using efficient computer graphics techniques," Appl. Opt. **57**, 7303–7313 (2018).
5. Z. Zhu and T. G. Brown, "Full-vectorial finite-diference analysis of microstructured optical fibers," Opt. Express **10**, 853–863 (2002).
6. K.-L. W. Yong-Jiu Zhao and K.-K. M. Cheng, "A compact 2-d full-wave finite-difference frequency-domain method for general guided wave structures," TRANSACTIONS ON MICROWAVE THEORY AND TECHNIQUES **50**, 1844–1848 (2002).
7. C.-P. Yu and H.-C. Chang, "Yee-mesh-based finite difference eigenmode solver with pml absorbing boundary conditions for optical waveguides and photonic crystal fibers," OPTICS EXPRESS **12**, 6165–6177 (2004).
8. M.-y. Chen, S.-m. Hsu, and H.-c. Chang, "A finite-difference frequency-domain method for full-vectroial mode solutions of anisotropic optical waveguides with an arbitrary permittivity tensor," Opt. Express **17**, 5965–5979 (2009).
9. C.-H. Du and Y.-P. Chiou, "Higher-order full-vectorial finite-difference analysis of waveguiding structures with circular symmetry," PHOTONICS TECHNOLOGY LETTERS **24**, 894–896 (2012).
10. Y.-P. Chiou and C.-H. Du, "Arbitrary-order interface conditions for slab structures and their applications in waveguide analysis," OPTICS EXPRESS **18**, 4088–4102 (2010).
11. Y.-P. Chiou and C.-H. Du, "Arbitrary-order full-vectorial interface conditions and higher order finite-difference analysis of optical waveguides," JOURNAL OF LIGHTWAVE TECHNOLOGY **29**, 3445–3452 (2011).
12. S. Sujecki, "Arbitrary truncation order three-point finite difference method for optical waveguides with stepwise refractive index discontinuities," OPTICS LETTERS **35**, 4115–4117 (2010).
13. Y. CAO, "Arbitrary-order three-point finite difference method for the modal analysis of chiral waveguides," OPTICS EXPRESS **30**, 4680–4691 (2022).
14. J. D. Jackson, *Classical electrodynamics* (JOHN WILEY & SONS INC, 1999).
15. S. G. Johnson and J. D. Joannopoulos, "Block-iterative frequency-domain methods for maxwell's equations in a planewave basis," Opt. express **8**, 173–190 (2001).
16. A. F. Oskooi, C. Kottke, and S. G. Johnson, "Accurate finite-difference time-domain simulation of anisotropic media by subpixel smoothing," OPTICS LETTERS **34**, 2778–2780 (2009).
17. D. Alexopoulos and T. Kamalakis, "pyfdfdsolver: Python tool for photonic simulations," github (2022), https://github.com/dalexopoulos83/pyfdfdsolver/blob/main/README.md.
18. K. Yee, "Numerical solution of initial boundary value problems involving maxwell's equations in isotropic media," IEEE Transactions on antennas propagation **14**, 302–307 (1966).
19. G. R. Werner and J. R. Cary, "A stable fdtd algorithm for non-diagonal, anisotropic dielectrics," J. Comput. Phys. **226**, 1085–1101 (2007).
20. R. B. Lehoucq, D. C. Sorensen, and C. Yang, *ARPACK users' guide: solution of large-scale eigenvalue problems with implicitly restarted Arnoldi methods* (SIAM, 1998).
21. A. W. Snyder and J. Love, *Optical waveguide theory* (Springer Science & Business Media, 2012).
22. T. Hasegawa, E. Sasaoka, M. Onishi, M. Nishimura, Y. Tsuji, and M. Koshiba, "Hole-assisted lightguide fiber for large anomalous dispersion and low optical loss," Opt. Express **9**, 681–686 (2001).
23. D. Chen, "Cylindrical hybrid plasmonic waveguide for subwavelength confinement of light," APPLIED OPTICS **49**, 6868–6871 (2010).